A VISUAL SURFACE DEFECT DETECTION METHOD BASED ON LOW RANK AND SPARSE REPRESENTATION

Jingang Cao[1,2], Guotian Yang[2], Xiyun Yang[2] and Jinhua Li[1]

[1]School of Control and Computer Engineering
North China Electric Power University
No. 689, Huadian Road, Lianchi District, Baoding 071003, P. R. China
caojg168@126.com

[2]School of Control and Computer Engineering
North China Electric Power University
No. 2, Beinong Road, Changping District, Beijing 102206, P. R. China

ABSTRACT. *Surface defect detection is very crucial for product quality control. A visual detection method based on low rank and sparse representation for surface defect detection of the wind turbine blade is brought forward in this paper. Two terms, which are the Laplacian regularization term and the noise term, were added into robust principal component analysis (RPCA). The noise term defined by F-norm is used to suppress uneven illumination and Gaussian noise, and the Laplacian regularization term is utilized to constrain the spatial relationship of superpixels. The defect image is considered to consist of a low rank matrix, a sparse matrix and a noise matrix, which corresponds with non-defect portion, defect portion and the noise portion of the image. At first, the proposed method segments the input image into a number of non-overlapping superpixels and extracts their features. Then, the optimal salient map is generated via the proposed method. Finally, the binary image is obtained by Otsu method. By quantitative and qualitative evaluation, experimental results illustrate that the proposed method is superior in terms of robustness and accuracy compared with 10 state-of-the-art methods on the synthetic and real images.*

Keywords: Surface defect detection, Visual saliency, Low rank and sparse representation, Computer vision, Robust principal component analysis

1. **Introduction.** As one of the most important renewable energies, wind energy has been exploited in many countries in recent years. The blade is an important component of wind turbine system; it is reported that the cost of blades accounts for 15-20% of the overall wind turbine cost [1]. Nowadays the wind turbine blade becomes larger and larger, blade damage is one of common types of damage in wind turbine system and its repair needs long time and is also very expensive. Therefore, condition inspection and defect detection of the blade have been vigorously researched to ensure the blade quality. The methods include vibration analysis, performance monitoring, acoustic emission, radiographic inspection, ultrasonic testing techniques, strain measurement, thermography, electrical effects, and so on [2]. These methods usually require special equipment or installation of a large number of sensors to inspect the blade in factory or before the blade is assembled into the wind turbine at the wind farm [3], and they are not suitable for routine inspection of wind turbine blade during the service at the wind farm. Employing unmanned aerial vehicles to inspect the surface condition of wind turbine blade has

been tried recently [4], because this method can capture images or videos of the blade to analyse whether there are defects or not through image processing approaches.

In fact, surface defect detection is very important for many industrial fields. The traditional surface defect detection methods mainly depend on observation via human eyes, and they are not only inefficient, time-consuming and laborious, but easily affected by personal and environmental factors. With the development of image processing technology, computer vision-based defect detection has been rapidly developed and has been applied in product quality monitoring, such as fabric [5], PCB printing plates [6], steel plates [7], solar cells [8] and TFT-LCD panels [9]. There are about three types of methods for surface defect detection: spatial statistical methods, spectral methods, and model-based methods. Spatial statistical methods utilize diverse statistical properties of defects to detect defects, but the detection results are susceptible to the shape and pattern of the defect. In addition, these methods cannot exploit the image's global information effectively, and detection results are prone to be influenced by noise. Spectral methods transform the image to the spectrum domain to discriminate defects, but their performance depends largely on the chosen filter. Model-based methods extract features of the defect through modeling and parameter estimation techniques. Defect detection is realized by discriminating whether the test image conforms with the normal model. Model-based methods could obtain satisfactory detection performance, but they are limited in real applications because of high computational complexity.

Saliency detection, as a promising research field, has been used in many situations, such as quality assessment [10], object recognition [11], image segmentation [12] and compression [13], and image retrieval [14]. The surface defect regions can be regarded as salient regions and non-defect regions can be seen as the background, so saliency detection methods can be applied to surface defect detection. The crucial work of saliency detection is to generate a salient map. Salient values of pixels or regions represent their salient degree in an image. The larger the value, the higher the salient degree. The computational complexity can be reduced by focusing on the salient regions.

Bottom-up and top-down models are the main methods for image saliency detection [15,16]. Top-down models are task-driven, which need to extract the visual information of an object and form a salient map through training and learning, and deep-learning based methods belong to top-down models. In contrast, bottom-up models explore low-level vision features to form a salient map, such as location, texture and colour. Thus, they are stimulus-driven. Some visual priors are utilized to enhance the accuracy, such as contrast prior [17], background prior [18] and center-dark channel prior [19]. Compared with the top-down models, bottom-up models have less computational complexity and better generality. Many researchers are devoted to the study of detecting image saliency. Itti et al. [20] present a visual attention system to generate salient maps via center and surround filter. Achanta et al. [21] propose a frequency-tuned method, which adopts colour and luminance features to estimate center-surround contrast. Although this method is simple and efficient, the salient map contains a large amount of background noise. Goferman et al. [22] put forward a context-aware saliency detection approach, but the salient map would contain parts of background. Jiang et al. [23] utilize an absorbing Markov chain to formulate image salient detection, and the saliency of a region hinges on its absorbed time. Yang et al. [24] adopt manifold ranking to rank the similarity of superpixels with foreground and background seeds. According to this model, Wang et al. [25] suggest detecting saliency by combining local graph structure and background priors together, so salient information among different nodes can be jointly exploited. However, a fully connected graph has high computational cost. Combining top-down learning methods and bottom-up contrast-based saliency models, Tong et al. [26] present a bootstrap learning

method to detect salient object, which generates training samples via a bottom-up model. Although these methods have achieved certain effects on saliency detection, there are still problems that salient regions are not obvious, incomplete and even have background noise. So sometimes it is difficult to distinguish salient regions from the background.

Low rank representation has been utilized to detect defects recently, which considers the defect image is composed of defect foreground and non-defect background, and these two portions can be expressed by a sparse matrix and a low rank matrix, respectively. Shen and Wu [27] combine low-level features and higher-level priori to detect salient object, and decompose an image into non-salient regions and salient regions represented by a low rank matrix and a sparse matrix. Based on robust principal component analysis (RPCA), Yao et al. [28] propose a method to detect solar cells surface defects, which transforms a pair of images into one matrix. This method requires all images must be collected under the same conditions. Huangpeng et al. [29] detect defects by a low-rank representation and texture prior. Cen et al. [9] apply low rank matrix reconstruction to TFT-LCD panels surface defect detection, but it does not consider the effect of noise and uneven illumination and can only deal with images with simple background. Cao et al. [30] detect fabric defects with NRPCA, which added a noise term to the RPCA model, but this approach cannot detect whole defect regions because of ignoring the connectivity of pixels. Zhou et al. [31] segment surface defect via a double low-rank and sparse decomposition method, which considers that the feature vectors of defect regions lie in a low-dimensional space and the defect regions are highly correlated, the defect feature matrix thus is low rank rather than sparse. However, this is not the case, when there are different types of defects in an image, the low rank property of defects could be broken. Therefore, the detection performance is poor for multi-region defects.

Inspired by the above approaches, a visual surface defect detection method combined low rank and sparse representation is proposed. The main contribution of our work can be summarized as follows. Firstly, a noise term is added to reduce the effect of noise and uneven illumination based on RPCA. Secondly, a Laplacian regularization term is applied to constrain the spatial relationship of superpixels, which is beneficial to detect whole defect regions. Through these two added terms, our method can detect surface defects more completely and accurately, and also can suppress uneven illumination and noise effectively. Finally, we test the method on the synthetic and real images.

The remainder of the paper is organized as follows. In Section 2, we elaborate the proposed method and the specific procedures. Section 3 describes the process of surface defect detection. In Section 4, we discuss the experimental results in detail. Finally, the conclusion is drawn in Section 5.

2. **The Proposed Method.** At present, researchers have done great efforts and already have made some progress in visual surface defect detection [5-9,27-31], but there are still some problems or difficulties about visual surface defect detection. As images are easily affected by environment, illumination, noise and so on, it is difficult to detect defects effectively when these factors change. How to construct a robust detection method to adapt to illumination changes, noise and other external environmental interference is one of the problems to be solved. At the same time, due to the variety of detection objects and defect types, and unclear relationship between the mechanism of defects and their external expressions, it is hard to effectively extract defect features, describe defects and their characteristics, which makes defect segmentation difficult. Our work is mainly to resolve the impact of noise and uneven illumination on the image and improve the robustness of defect detection method.

In this section, we elaborate the principle of surface defect detection based on low rank and sparse representation.

2.1. **RPCA method.** According to RPCA [32], the feature matrix of an image D can be decomposed into a low rank matrix L and a sparse matrix S, which can be expressed as

$$D = L + S \tag{1}$$

Equation (1) can be described as one optimization problem as follows:

$$\begin{cases} \min\limits_{L,S} \ (rank(L) + \lambda \, \|S\|_0) \\ \text{s.t.} \ \ D = L + S \end{cases} \tag{2}$$

where $rank(\cdot)$ represents the rank of a matrix; $\|\cdot\|_0$ is the l_0 norm of a matrix. Formula (2) is relaxed to a following convex optimization problem for it is an NP-hard problem.

$$\begin{cases} \min\limits_{L,S} \ (\|L\|_* + \lambda \, \|S\|_1) \\ \text{s.t.} \ \ D = L + S \end{cases} \tag{3}$$

where $\|\cdot\|_*$ is a convex relaxation of $rank(\cdot)$ and denotes the nuclear norm of a matrix, which is equal to the sum of the singular values of a matrix. $\|\cdot\|_1$ represents the l_1 norm of a matrix, which is equal to the sum of the absolute values of all elements of a matrix. $\lambda > 0$ is used to balance L and S. The detection performance of RPCA is poor because it cannot detect the whole defect region and has a large amount of noise.

2.2. **The proposed method based on RPCA.** All regions of the background are usually strongly correlated and located in a low-dimensional subspace, the background thus can be characterized by a low rank matrix. However, defect regions are different from the background and can be regarded as the salient object, which can be characterized by a sparse matrix. In order to detect continuous defect regions, suppress noise, and reduce the influence of uneven illumination, the F-norm term is added to suppress uneven illumination and noise, and the Laplacian regularization term is used to constrain the spatial relationship of pixels or superpixels, which is beneficial to detect continuous defect regions. The model can be expressed as follows:

$$\begin{cases} \min\limits_{L,S,G} \ \left(rank(L) + \lambda \, \|S\|_0 + \beta\Theta(L,S) + \frac{\gamma}{2} \, \|G\|_F^2\right) \\ \text{s.t.} \ \ D = L + S + G \end{cases} \tag{4}$$

where $D, L, S, G \in R^{N \times K}$ represent the feature matrix, the low rank matrix, the sparse matrix and the noise matrix, respectively. N and K denote the number of features and superpixels, respectively. $\|\cdot\|_F$ is the F-norm of a matrix; λ, β and γ are regularization parameters, and they are all larger than zero; $\Theta(L,S)$ represents the Laplacian regularization term, and it can keep the local consistency and invariance among the spatially adjacent superpixels which have similar salient values in a salient map. The Laplacian regularization term is beneficial to the segmentation of defects and can segment defects from the background as much as possible.

$$\Theta(S,L) = \frac{1}{2}\sum_{i,j=1}^{K} \|s_i - s_j\|_2^2 w_{ij} = tr\left(SMS^T\right) \tag{5}$$

$$w_{ij} = \begin{cases} \exp\left(\frac{-\|p_i - p_j\|_2^2}{2\sigma^2}\right), & p_i \text{ and } p_j \text{ are adjacent superpixels} \\ 0, & \text{otherwise} \end{cases} \tag{6}$$

where $tr(\cdot)$ is the trace of a matrix; $w_{ij} \in W$, $W \in R^{K \times K}$, W is the weight matrix and it represents the feature similarity among all of superpixels. $\|p_i - p_j\|_2^2$ represents the Euclidean distance between average colour of superpixels p_i and p_j in CIELAB; σ is a scalar; $M \in R^{K \times K}$ is the Laplacian matrix.

$$M_{ij} = \begin{cases} -w_{ij}, & i \neq j \\ \sum_{i \neq j} w_{ij}, & \text{otherwise} \end{cases} \tag{7}$$

By using $\|\cdot\|_*$ and $\|\cdot\|_1$ to replace $rank(\cdot)$ and $\|\cdot\|_0$, Equation (4) becomes the following convex optimization problem.

$$\begin{cases} \min_{L,S,G} \left(\|L\|_* + \lambda \|S\|_1 + \beta \Theta(L,S) + \frac{\gamma}{2} \|G\|_F^2 \right) \\ \text{s.t.} \quad D = L + S + G \end{cases} \tag{8}$$

By introducing an auxiliary variable H, and let $H = S$, then

$$\begin{cases} \min_{L,S,G,H} \left(\|L\|_* + \lambda \|S\|_1 + \beta tr \left(HMH^T \right) + \frac{\gamma}{2} \|G\|_F^2 \right) \\ \text{s.t.} \quad D = L + S + G, \ H = S \end{cases} \tag{9}$$

Its augmented Lagrangian function is expressed as:

$$\begin{aligned} &O(L,S,G,H,Y_1,Y_2,\mu) \\ &= \min \left(\|L\|_* + \lambda \|S\|_1 + \beta tr \left(HMH^T \right) + \frac{\gamma}{2} \|G\|_F^2 + tr \left(Y_1^T (D - L - S - G) \right) \right. \\ &\quad \left. + tr \left(Y_2^T (H - S) \right) + \frac{\mu}{2} \|D - L - S - G\|_F^2 + \frac{\mu}{2} \|H - S\|_F^2 \right) \end{aligned} \tag{10}$$

where Y_1 and Y_2 are Lagrange multipliers, $\mu > 0$ is a regularization parameter. Thus, Equation (10) can be rewritten as follows:

$$\begin{aligned} &O(L,S,G,H,Y_1,Y_2,\mu) \\ &= \min \left(\frac{1}{\mu} \|L\|_* + \frac{\lambda}{\mu} \|S\|_1 + \frac{\beta}{\mu} tr \left(HMH^T \right) + \frac{\gamma}{2\mu} \|G\|_F^2 \right. \\ &\quad \left. + \frac{1}{2} \left\| D - L - S - G + \frac{Y_1}{\mu} \right\|_F^2 + \frac{1}{2} \left\| H - S + \frac{Y_2}{\mu} \right\|_F^2 \right) \end{aligned} \tag{11}$$

The ADMM [33] algorithm is used to solve H, L, S and G.

Updating H: To update H with fixed L, S and G

$$\min_H \left(\frac{1}{2} \left\| H - S + \frac{Y_2}{\mu} \right\|_F^2 + \frac{\beta}{\mu} tr \left(HMH^T \right) \right) \tag{12}$$

For the derivative of (12) with respect to H, set it equal to zero, and the solution can be calculated as:

$$H = \left(S - \frac{Y_2}{\mu} \right) \left(I + \frac{2\beta}{\mu} M \right)^{-1} \tag{13}$$

Updating L: To update L with fixed H, S and G

$$\min_L \left(\frac{1}{\mu} \|L\|_* + \frac{1}{2} \left\| \left(D - S - G + \frac{Y_1}{\mu} \right) - L \right\|_F^2 \right) \tag{14}$$

The solution is

$$L = U \Psi_{\frac{1}{\mu}}(\Sigma) V^T \tag{15}$$

where $(U, \Sigma, V) = svd\left(D - S - G + \frac{Y_1}{\mu}\right)$, $svd(\cdot)$ denotes singular value decomposition.

$$\Psi_{\frac{1}{\mu}}(T) = sgn(T) \cdot \max\left(|T| - \frac{1}{\mu}, 0\right) = \begin{cases} T_{ij} - \frac{1}{\mu}, & T_{ij} > \frac{1}{\mu} \\ 0, & -\frac{1}{\mu} \leq T_{ij} \leq \frac{1}{\mu} \\ T_{ij} + \frac{1}{\mu}, & T_{ij} < -\frac{1}{\mu} \end{cases} \quad (16)$$

Updating S: Fix H, L, G and update S

$$\min_S \left(\frac{\lambda}{\mu}\|S\|_1 + \frac{1}{2}\left\|\left(D - L - G + \frac{Y_1}{\mu}\right) - S\right\|_F^2 + \frac{1}{2}\left\|\left(H + \frac{Y_2}{\mu}\right) - S\right\|_F^2\right) \quad (17)$$

It can be expressed as follows:

$$\min_S \left(\frac{\lambda}{4\mu}\|S\|_1 + \frac{1}{2}\left\|\frac{1}{2}\left(D + H - L - G + \frac{Y_1 + Y_2}{\mu}\right) - S\right\|_F^2\right) \quad (18)$$

The solution is

$$S = \Psi_{\frac{\lambda}{4\mu}}\left[\frac{1}{2}\left(D + H - L - G + \frac{Y_1 + Y_2}{\mu}\right)\right] \quad (19)$$

Updating G: To update G with fixed H, L and S

$$\min_G \left(\frac{\gamma}{2\mu}\|G\|_F^2 + \frac{1}{2}\left\|D - L - S - G + \frac{Y_1}{\mu}\right\|_F^2\right) \quad (20)$$

With respect to G, take the derivative of (20) and set it to be zero, the solution is

$$G = \frac{\mu(D - L - S) + Y_1}{\gamma + \mu} \quad (21)$$

Updating Y_1, Y_2 **and** μ:

$$Y_1 = Y_1 + \mu(D - L - S - G) \quad (22)$$

$$Y_2 = Y_2 + \mu(H - S) \quad (23)$$

$$\mu = \min(\rho\mu, \mu_{\max}), \ \rho > 0 \quad (24)$$

The algorithm can be described as follows.

Input: Feature matrix D

Output: Low rank matrix L, sparse matrix S and noise matrix G

Step 1: Initialize $L = S = G = H = 0$, $Y_1 = Y_2 = 0$ and related parameters $\lambda = 0.03$, $\beta = 0.01$, $\gamma = 0.05$, $K = 300$, $\rho = 1.1$, $\mu_{\max} = 1e+10$, $\varepsilon = 1e\text{-}7$, $\mu = 0.1$ and $k_{\max} = 1000$.

Step 2: Update H, L, S, and G according to Formulas (13), (15), (19) and (21).

Step 3: Update Y_1, Y_2 and μ according to Formulas (22) $\sim$ (24).

Step 4: Determine whether the maximum number of iterations $k_{\max}$ is reached or error is less than ε. If yes, then output L, S, G and finish; Otherwise, update the number of iterations and go to Step 2.

Combined low rank and sparse representation, this algorithm can improve the accuracy of defect detection by adding a noise term and considering the correlation between non-defect portions and defect portions. It also has strong robustness to uneven illumination and noise.

3. **Defect Detection Process.** In this section, we introduce surface defect segmentation based on the proposed method. Figure 1 is the framework of surface defect detection for wind turbine blade.
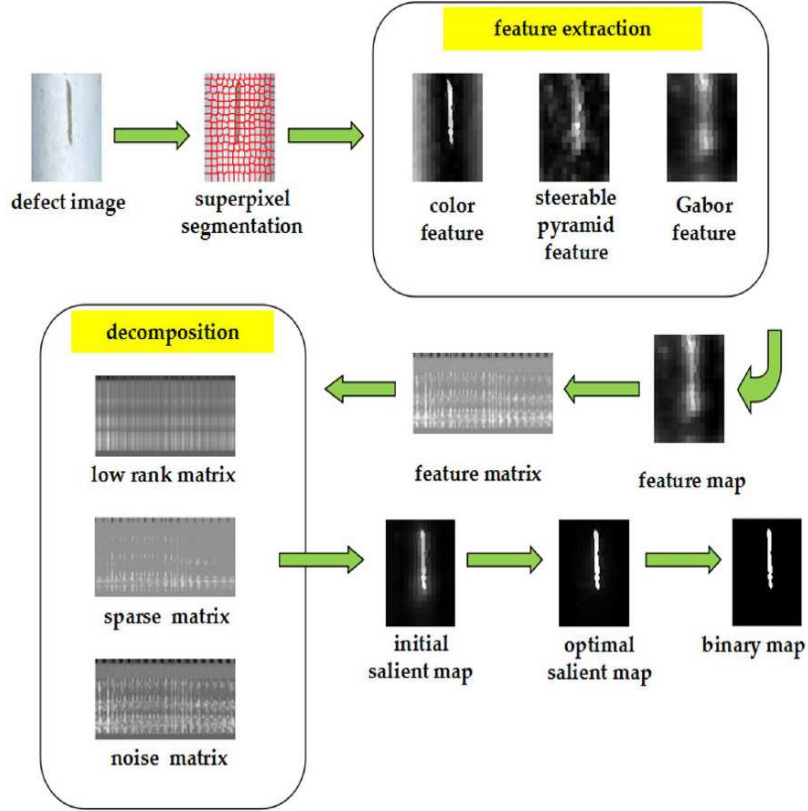
FIGURE 1. The framework of surface defect detection

3.1. **Superpixel segmentation.** The surface defect portion and the non-defect portion of wind turbine blades have different characteristics, such as colour and texture. We first partition an input defect image I into K non-overlapping superpixels $P = \{p_1, p_2, \ldots, p_k\}$ via SLIC algorithm [34].

3.2. **Feature extraction.** Each superpixel is an N-dimension feature vector and can be denoted as $d_i \in R^N$. We extract colour feature, Gabor feature and steerable pyramid feature of an image according to [27]. The image feature matrix $D = \{d_1, d_2, \ldots, d_K\} \in R^{N \times K}$.

Colour feature: We extract three colour values of the red, green and blue combining with the hue and the saturation of HSV colour space to form colour feature. The average colour feature of pixels which belong to the same superpixel is defined as colour feature of this superpixel.

Gabor feature: Gabor filters are particularly fit for texture description and discrimination because the frequency and direction of Gabor filters are similar to the human visual system. We employ Gabor filters with 12 directions on 3 different scales to yield 36 filter responses for each pixel.

Steerable pyramid feature: We utilize steerable pyramids filters with 6 directions on 2 different scales to yield 12 filter responses for each pixel.

3.3. **Generating the salient map via the proposed method.** According to the proposed method, the input image feature matrix D is decomposed into three components: L, S and G. According to the obtained sparse matrix $S = \{s_1, s_2, \ldots, s_k\}$, salient values of superpixels can be calculated as follows:

$$a_i = \|s_i\|_1, \ i = 1, 2, \ldots, K \tag{25}$$

where a_i represents the salient value of superpixel p_i, s_i denotes the ith column of S, $\|\cdot\|_1$ represents the l_1 norm of a vector. The larger a_i, the greater the probability that the superpixel is a salient portion. And now, a salient map of the input image is constructed. From the initial salient map of Figure 1, it is seen that our proposed method can suppress the uneven illumination and noise effectively, and it also can improve the accuracy of surface defect detection.

3.4. **The optimization of salient map.** In order to enhance the salient map, the optimization method [35] is adopted. The cost function is defined as:

$$\min_{a_i} \left(\sum_{i=1}^{K} w_i^b a_i^2 + \sum_{i=1}^{K} w_i^f (a_i - 1)^2 + \sum_{i,j=1}^{K} w_{ij} (a_i - a_j)^2 \right) \tag{26}$$

where w_i^b is the salient value of superpixel p_i in the background image, w_i^f is the salient value of superpixel p_i in the foreground image, which can be obtained according to Equation (25). Formula (26) can be rewritten as follows:

$$\min_{A} \left(A^T W^b A + A^T W^f A - 2W^f A + W^f I + 2A^T M A \right) \tag{27}$$

where $A = (a_1, a_2, \ldots, a_K)^T$, $W^b = diag\left[\left(w_1^b, w_2^b, \ldots, w_K^b\right)^T \right] \in R^{K \times K}$, $W^f = diag\left[\left(w_1^f, w_2^f, \ldots, w_K^f\right)^T \right] \in R^{K \times K}$, $diag(\cdot)$ represents a diagonal matrix, $M \in R^{K \times K}$ is the Laplacian matrix, $I \in R^{K \times 1}$ is a one vector. By taking the derivative of (27) with respect to A and setting it to be zero, the solution is

$$A = \left(W^f + W^b + 2M \right)^{-1} W^f I \tag{28}$$

Through optimization, the salient values of defect regions are increased, and the salient values of non-defect regions are reduced, so the salient map of the defect object is improved.

3.5. **Defect segmentation.** Finally, Otsu algorithm [36] is performed on the salient map. Otsu algorithm is a clustering method, and it divides gray levels of an image into two classes, which has the maximum between-class variance and the minimum within-class variance. Ostu algorithm can be used to automatically select the optimal threshold for binarization, and it can obtain the minimum error probability of classification. See the binary image of Figure 1, and white pixels denote surface defects.

4. **Experimental Results and Analysis.** In order to evaluate the performance of our proposed method, a synthetic dataset including 282 images was constructed. This synthetic experiment focuses on the robustness of methods under uneven illumination and Gaussian noise. We select 10 state-of-the-art methods including RPCA [32], NRPCA [30], WLRR [37], DLRSD [31], Wavelet [38], SR [39], FF [40], CA [22], GMR [24] and SROD [41] to compare with our method. Among them, RPCA, NRPCA, WLRR and DLRSD are low rank represent methods. SR is the spectral residual approach. FF denotes salient region detection method via fusing bottom-up and top-down features; CA represents the context-aware saliency method; Wavelet uses wavelet transform to extract low-level features and then detect image saliency; GMR adopts graph-based manifold ranking to detect saliency; SROD is a saliency detection by sparse residual and outlier detection. These methods use default parameters that authors set in their source codes. We adopt these methods to detect surface defect of wind turbine blade. The simulation environment is: operating system is Windows 10, simulation software is MATLAB R2017b, CPU is Intel (R) i5 3.6 GHz and RAM is 16 GB.

4.1. **Parameter settings.** In Equation (4), there are three parameters λ, β and γ in our model, and we also discuss how to select the number of superpixels K. We tune their values to carry out some experiments and test the detection performance of the proposed method. We select their values according to weighted F_β^w-measure (WF) [42]. Figure 2 shows the relationship among parameters. When $\lambda \in [0.01, 0.05]$, $\beta \in [0.005, 0.1]$, $\gamma \in [0.05, 0.1]$, $K \in [250, 300]$, WF can attain a better value. In our experiments, we set $\lambda = 0.03$, $\beta = 0.01$, $\gamma = 0.05$ and $K = 300$, which can achieve much better segmentation results.
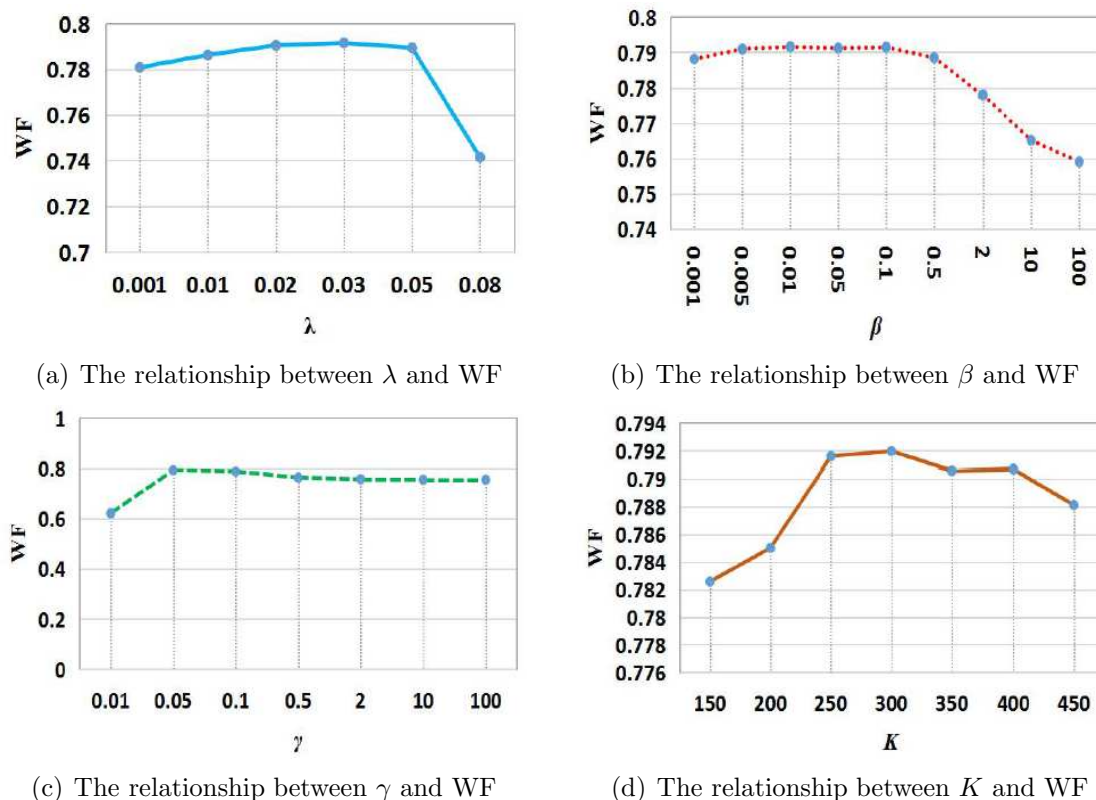

(a) The relationship between λ and WF

(b) The relationship between β and WF

(c) The relationship between γ and WF

(d) The relationship between K and WF

FIGURE 2. The relationship among parameters

4.2. **Qualitative comparison.** To analyse the performance of each method, the synthetic experiment is divided into three groups. In the first group, the defect images are under uniform illumination, and Figure 3 displays part of detection results. The defect images are under uneven illumination in the second group, Figure 4 shows part of detection results of this group. In the last group, we add Gaussian noise into defect images, in which SNR is from 10dB to 50dB, and some results are shown in Figure 5.

From Figure 3, we can see that RPCA and NRPCA have similar detection results, and they can detect part of defects, but the border of defects is not accurate, and sometimes fail to identify the square defect regions. DLRSD cannot uniformly highlight multiple defects, so it would miss some defects in the final binary image. The salient maps obtained by Wavelet contain a large amount of noise, and defect regions are difficult to be distinguished. In some case, GMR cannot detect whole defect regions and the border of defect is not accurate. For SROD, the salient maps are blurred, incomplete and inaccuracy. Although the salient maps have some differences, SR, FF and CA can only detect the border of defects. WLRR and our proposed method have the better detection results, and both can detect defects completely and accurately.
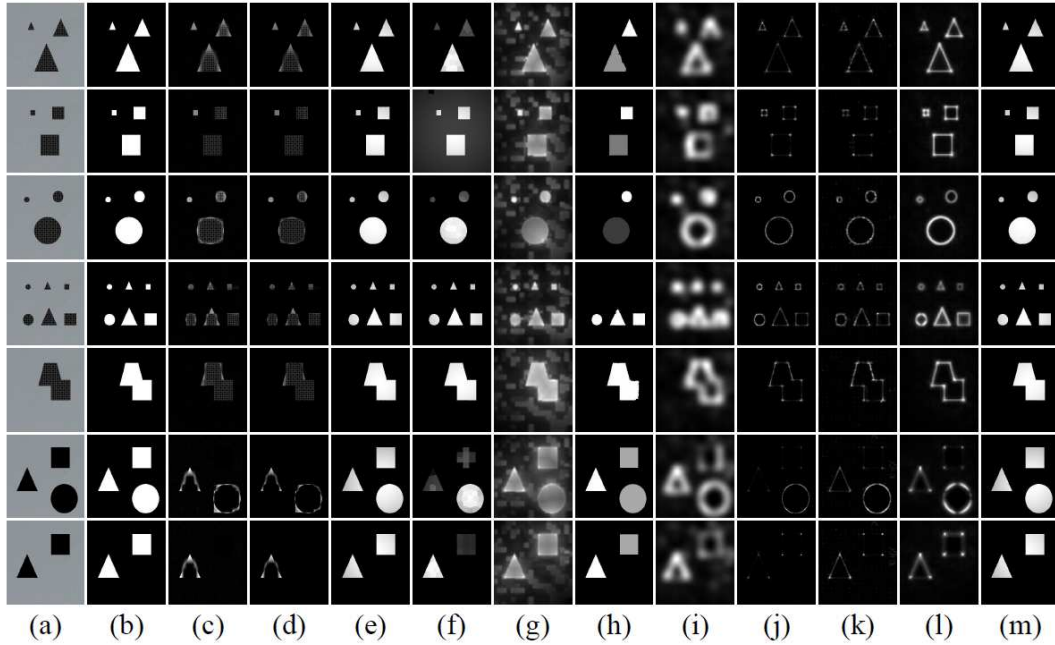
FIGURE 3. Comparison under uniform illumination. (a) Original image; (b) ground-truth; (c) RPCA; (d) NRPCA; (e) WLRR; (f) DLRSD; (g) Wavelet; (h) GMR; (i) SROD; (j) SR; (k) FF; (l) CA; (m) our proposed method.
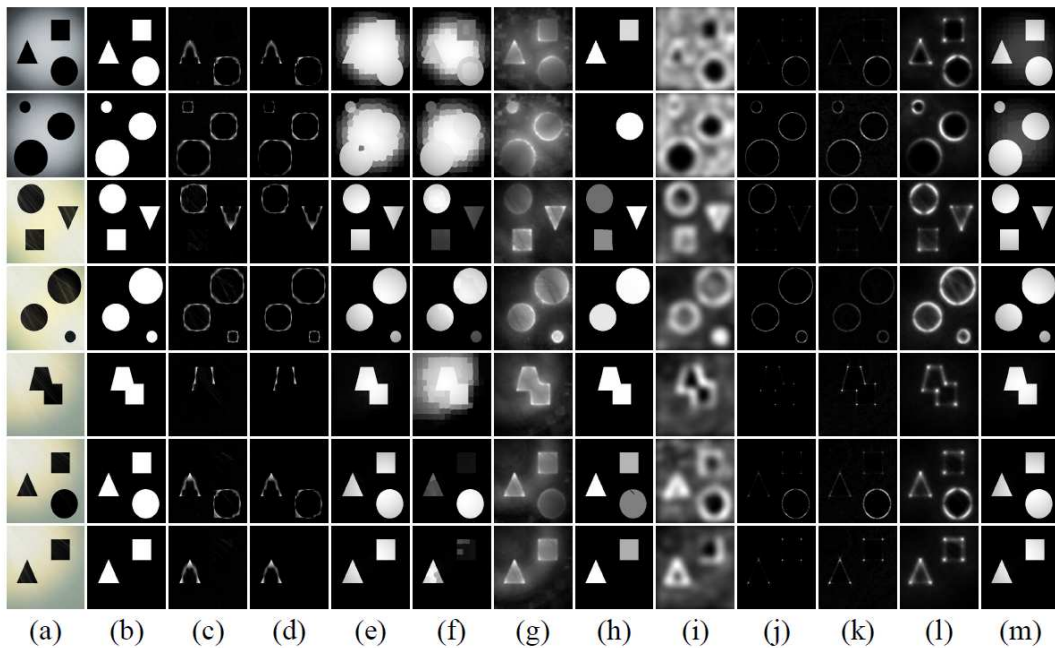

FIGURE 4. Comparison under uneven illumination. (a) Original image; (b) ground-truth; (c) RPCA; (d) NRPCA; (e) WLRR; (f) DLRSD; (g) Wavelet; (h) GMR; (i) SROD; (j) SR; (k) FF; (l) CA; (m) our proposed method.

It can be concluded from Figure 4 that salient maps obtained by RPCA and NRPCA just have part of defects border and it is not accurate, the square defect cannot be detected. WLRR and DLRSD could not detect effectively in the condition of row 1 and 2, and DLRSD cannot detect whole defects when there are multiple defect regions. SROD
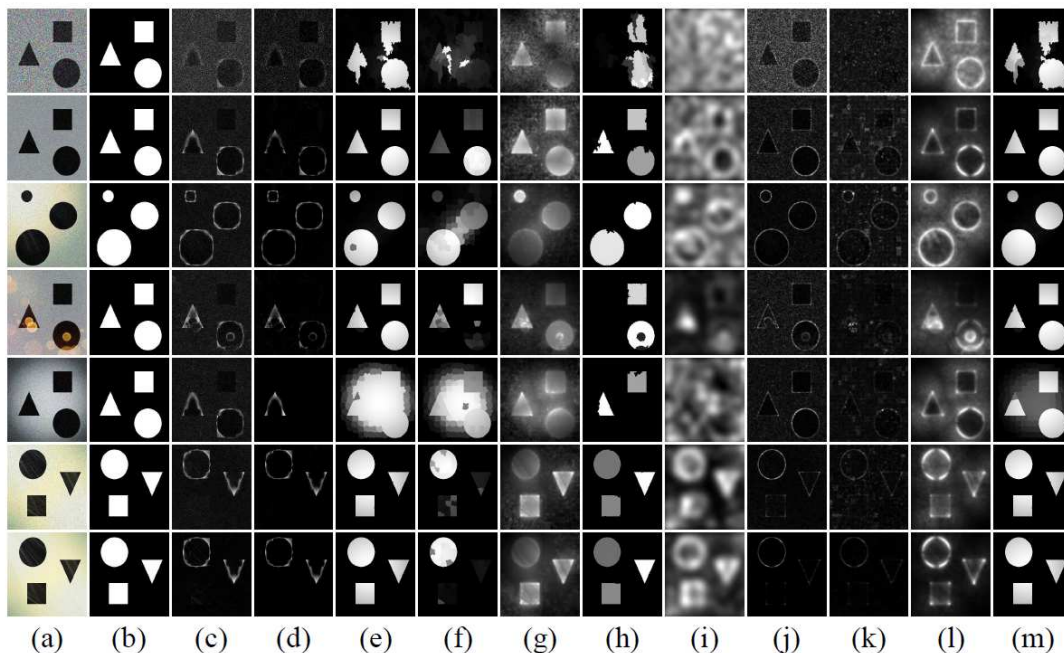
FIGURE 5. Comparison with different SNR values. (a) Original image; (b) ground-truth; (c) RPCA; (d) NRPCA; (e) WLRR; (f) DLRSD; (g) Wavelet; (h) GMR; (i) SROD; (j) SR; (k) FF; (l) CA; (m) our proposed method.

perform badly, the salient maps are blurred and contain a lot of noise, and it is difficult to distinguish defects form background. As for Wavelet, results have serious halo effect. GMR misses detecting some defects when an image contains multiple defects. And SR, FF and CA can only detect the border of defects, and results become worse than uniform illumination. Although uneven illumination has a certain influence on the salient map, our method achieves better results and could detect defects completely and accurately.

It can be seen from Figure 5 that all methods cannot detect defects effectively when SNR = 10 dB (e.g., row 1). When SNR = 20 dB (e.g., row 2, 3, 4, 5 and 6), RPCA and NRPCA could detect the approximate border of defects, but NRPCA can suppress noise better. WLRR and DLRSD cannot detect defects effectively in some conditions (e.g., row 3 and 5). DLRSD and GMR could miss detecting some defects when there are multiple defects. The rest methods, such as SROD, SR, FF, CA and Wavelet, are unable to perform effective detection. This is because they could not suppress Gaussian noise and the salient maps contain a large amount of noise. Although the noise has a certain influence on results (e.g., row 4 and 5), the proposed method achieves better detection performance among all methods. When SNR $\geq$ 30 dB, the noise has a little influence on the detection results of each method.

From the above results, it can be found that the proposed method has attained better detection performance whether under uneven illumination or in Gaussian noise.

4.3. **Quantitative comparison.** We adopt six quantitative metrics to analyse the performance of each method: precision-recall (PR) curve, F-measure curve, area under the receiver operation characteristic (AUC), weighted F_{β}^{w}-measure (WF), mean absolute error (MAE) and overlapping ratio (OR).

The definitions of precision rate (P), recall rate (R), false positive rate (FPR), true positive rate (TPR), OR and MAE are as follows:

$$P = \frac{TP}{TP + FP} \tag{29}$$

$$R = \frac{TP}{TP + FN} \tag{30}$$

$$FPR = \frac{FP}{FP + TN} \tag{31}$$

$$TPR = \frac{TP}{TP + FN} \tag{32}$$

$$OR = \frac{|S \cap G|}{|S \cup G|} \tag{33}$$

$$MAE = \frac{\sum_{l=1}^{H} \sum_{m=1}^{W} |S(l,m) - G(l,m)|}{H \times W} \tag{34}$$

where TP, TN, FP and FN represent the number of true positives, true negatives, false positives and false negatives in a salient map, respectively. A pixel is seen as a positive sample when it belongs to the defect; otherwise, a pixel is seen as a negative sample. S denotes the salient map and G is the ground-truth. H denotes the height of the input image and W represents the width of the input image.

By setting a series of discrete threshold within range $[0, 255]$, PR curve can be obtained on a grayscale salient map. A method achieves the better performance when its PR curve is closer to the upper left. Figure 6(a) shows PR curves of all methods. We can make the conclusion that the proposed method has attained better performance than other methods. For P and R cannot evaluate the performance comprehensively, F-measure is used, which is defined as

$$F = \frac{(1 + \beta^2) P \times R}{\beta^2 P + R} \tag{35}$$

where $\beta^2 = 0.3$ to emphasize precision [21]. From Figure 6(b), it can be seen that the proposed method has a higher F-measure value in many cases. We can come to the conclusion that our method outperforms other methods, and it also demonstrates the effectiveness of our method.

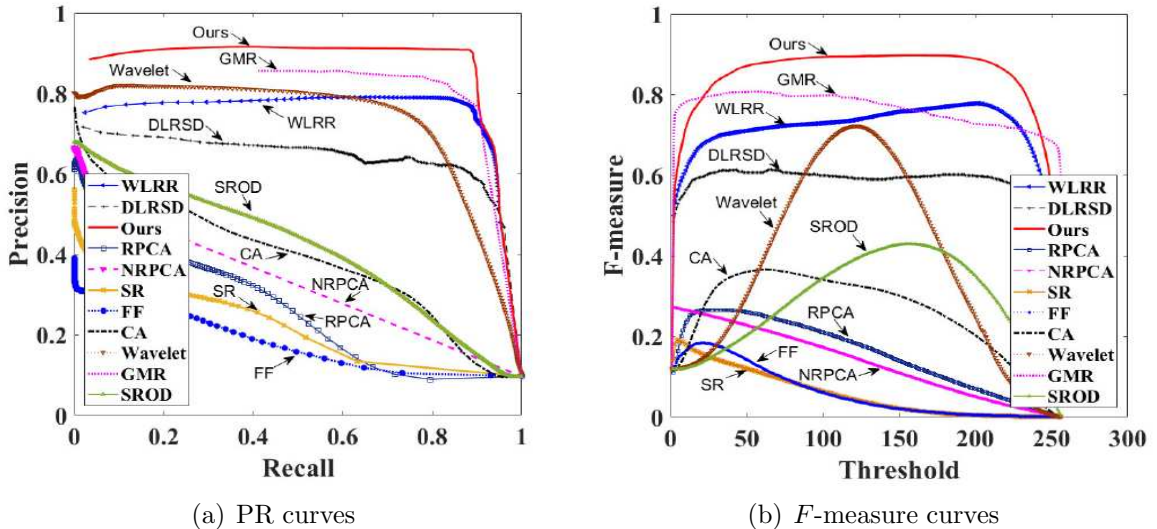(a) PR curves   (b) F-measure curves

FIGURE 6. The performance curves of all methods

The results of all methods on MAE, WF, AUC and OR are listed in Table 1. The optimal results are marked in bold, and the sub-optimal results are marked in italics. It can be shown that our method has achieved the best performance in MAE, WF and OR. Compared with GMR, the proposed method decreased by 3.24% in MAE, increased by 6.55% and 11.83% in WF and OR, respectively. AUC of our method is smaller than Wavelet, but larger than other methods. However, the other metrics of Wavelet are not good.

TABLE 1. Results of all methods on MAE, WF, AUC and OR

Methods	MAE ↓	WF ↑	AUC ↑	OR ↑
WLRR	0.09087	0.66460	0.88540	0.68752
DLRSD	0.11131	0.52601	0.86008	0.59416
RPCA	0.14577	0.12909	0.55609	0.14508
NRPCA	0.10601	0.11814	0.54695	0.12993
SR	0.14029	0.05745	0.49647	0.09432
FF	0.13155	0.06608	0.52401	0.09386
CA	0.17111	0.18223	0.78815	0.30352
Wavelet	0.19462	0.22748	**0.91014**	0.55422
GMR	*0.05669*	*0.72644*	0.85861	*0.74571*
SROD	0.27906	0.16793	0.77667	0.27412
Ours	**0.02432**	**0.79196**	*0.90136*	**0.86397**

Through the above qualitative and quantitative evaluation, we can conclude that our proposed method is more effective in suppressing Gaussian noise and uneven illumination than other 10 state-of-the-art methods and has the best detection performance.

At last, we adopt all methods to surface defect detection of wind turbine blade, and the dataset includes 34 defective images and their ground-truth. Figure 7 shows some results of surface defect detection of wind turbine blades.

From Figure 7, the similar conclusions can be drawn as in the synthetic experiment. RPCA and NRPCA can only detect part of defects border roughly. Results in RPCA contain a great deal of noise, and NPRCA can suppress noise because of the noise term. However, both of them cannot detect surface defects effectively because they do not consider the relationship of superpixels and cannot suppress the effect of the uneven illumination. The defect regions are not correct in row 1 and 2. WLRR cannot detect defect regions effectively in the uneven illumination (e.g., row 1 and 2), and DLRSD cannot detect complete defect regions in many cases. These four methods based on low rank representation cannot detect defects effectively because they do not consider the noise and the relationship of superpixels simultaneously. For Wavelet, SROD and CA, the border of defects is blurred and results have a large amount of background noise. GMR perform badly in many cases (e.g., row 2 to 6). SR and FF are unable to perform effective detection because it is difficult to identify defects from their results. Our proposed method can detect defects completely and accurately and achieves superior performance among all methods.

PR curves and F-measure curves of all methods are shown in Figure 8(a) and Figure 8(b), respectively. We can see that our proposed method has the best performance. According to Table 2, AUC of our method is less than Wavelet and bigger than other methods, but the results of Wavelet in visualized detection are not ideal and the defect regions are difficult to identify. As to the other metrics such as MAE, WF and OR, Table 2 shows that our method has obtained the best performance. Compared with NRPCA,
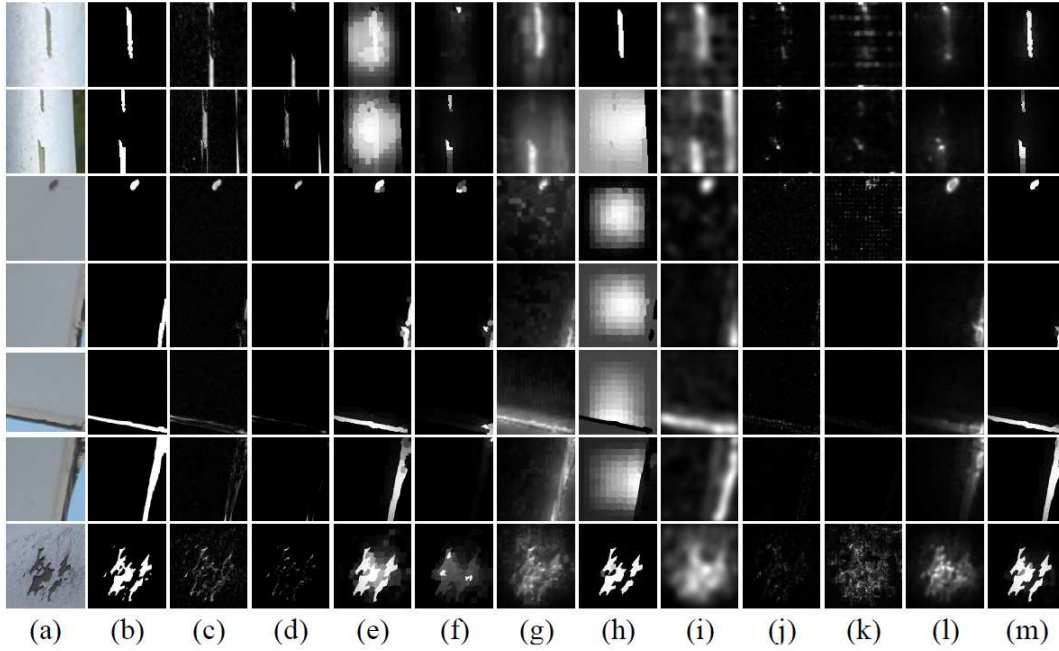
FIGURE 7. Surface defect detection results of wind turbine blades. (a) Original image; (b) ground-truth; (c) RPCA; (d) NRPCA; (e) WLRR; (f) DLRSD; (g) Wavelet; (h) GMR; (i) SROD; (j) SR; (k) FF; (l) CA; (m) our proposed method.

(a) PR curves   (b) *F*-measure curves
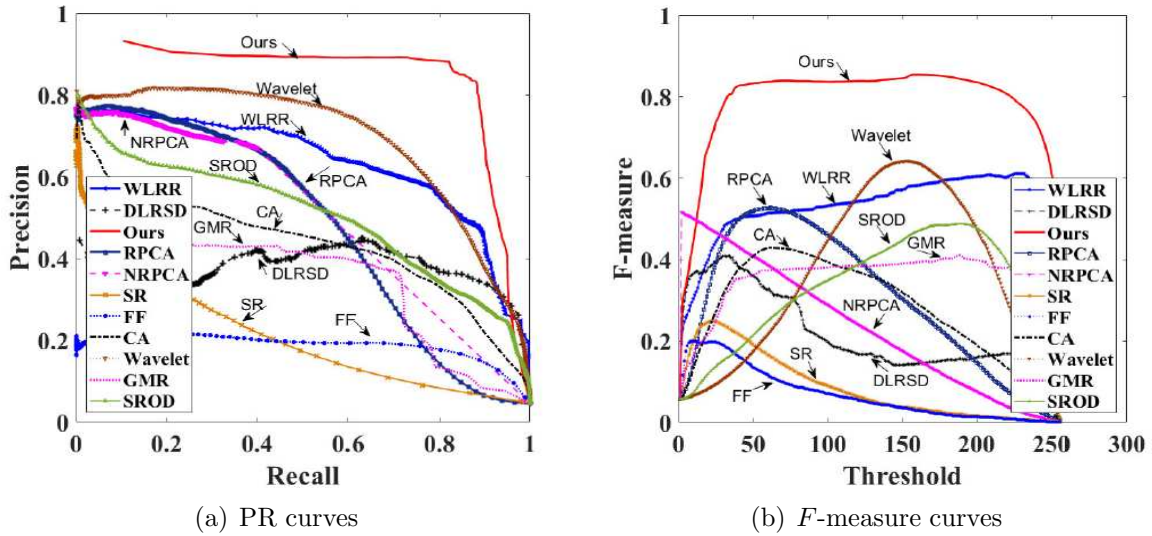
FIGURE 8. The performance curves of all methods

the proposed method decreased by 2.55% in MAE. Compared with WLRR, our method increased by 23.59% and 17.63% in WF and OR, respectively.

5. **Conclusion.** In this paper, combined visual saliency detection and RPCA, a method for detecting surface defects of wind turbine blades is proposed. Uneven illumination and Gaussian noise can be suppressed effectively by adding a noise term and a Laplacian regularization term to basic RPCA model. Through the experiments, we can draw the conclusion that the proposed method has better performance and higher accuracy for the surface defect detection of wind turbine blade compared with other 10 approaches.

TABLE 2. Results of all methods on MAE, WF, AUC and OR

Methods	MAE ↓	WF ↑	AUC ↑	OR ↑
WLRR	0.088607	*0.46557*	0.89555	*0.42554*
DLRSD	0.065056	0.22325	0.79470	0.34755
RPCA	0.067646	0.17451	0.79053	0.20433
NRPCA	*0.047874*	0.23600	0.64455	0.34203
SR	0.057428	0.08796	0.59005	0.12787
FF	0.064575	0.08930	0.62730	0.17600
CA	0.080609	0.17901	0.89149	0.25079
Wavelet	0.170440	0.14315	**0.94744**	0.30638
GMR	0.287420	0.23988	0.65540	0.38679
SROD	0.158890	0.17490	0.92190	0.24314
Ours	**0.022377**	**0.70143**	*0.92326*	**0.60183**

REFERENCES

[1] C. Ciang, J. Lee and H. Bang, Structural health monitoring for a wind turbine system: A review of damage detection methods, *Measurement Science and Technology*, vol.19, no.12, pp.1-20, 2008.

[2] F. García Márquez, A. Tobias, J. Pinar Pérez and M. Papaelias, Condition monitoring of wind turbines: Techniques and methods, *Renewabel Energy*, vol.46, pp.169-178, 2012.

[3] X. Li, J. Sun, N. Tao et al., An effective method to inspect adhesive quality of wind turbine blades using transmission thermography, *Journal of Nondestructive Evaluation*, vol.37, no.2, article 19, 2018.

[4] L. Wang and Z. Zhang, Automatic detection of wind turbine blade surface cracks based on UAV-taken images, *IEEE Transactions on Industrial Electronics*, vol.64, no.9, pp.7293-7303, 2017.

[5] M. Ng, H. Ngan, X. Yuan and W. Zhang, Patterned fabric inspection and visualization by the method of image decomposition, *IEEE Transactions on Automation Science and Engineering*, vol.11, no.3, pp.943-947, 2014.

[6] A. Crispin and V. Rankov, Automated inspection of PCB components using a genetic algorithm template-matching approach, *International Journal of Advanced Manufacturing Technology*, vol.35, nos.3-4, pp.293-300, 2007.

[7] J. Yun, D. Kim, K. Kim et al., Vision-based surface defect inspection for thick steel plates, *Optical Engineering*, vol.56, no.5, pp.1-12, 2017.

[8] W. Brooks, D. Lamb and S. Irvine, IR reflectance imaging for crystalline Si solar cell crack detection, *IEEE Journal of Photovoltaics*, vol.5, no.5, pp.1271-1275, 2017.

[9] Y. Cen, R. Zhao, L. Cen et al., Defect inspection for TFT-LCD images based on the low-rank matrix reconstruction, *Neurocomputing*, vol.149, Part C, pp.1206-1215, 2015.

[10] K. Gu, S. Wang, H. Yang et al., Saliency-guided quality assessment of screen content images, *IEEE Transactions on Multimedia*, vol.18, no.6, pp.1098-1110, 2016.

[11] Z. Ren, S. Gao, L. Chia and I. Tsang, Region-based saliency detection and its application in object recognition, *IEEE Transactions on Circuits and Systems for Video Technology*, vol.24, no.5, pp.769-779, 2014.

[12] Z. Tao, H. Liu, H. Fu and Y. Fu, Image cosegmentation via saliency-guided constrained clustering with cosine similarity, *Proc. of AAAI Conference on Artificial Intelligence*, San Francisco, CA, USA, pp.4285-4291, 2017.

[13] L. Duan, C. Ke, C. Wu et al., A natural image compression approach based on independent component analysis and visual saliency detection, *Journal of Computational and Theoretical Nanoscience*, vol.6, no.1, pp.385-388, 2012.

[14] Y. Gao, M. Shi, D. Tao and C. Xu, Database saliency for fast image retrieval, *IEEE Transactions on Multimedia*, vol.17, no.3, pp.359-369, 2015.

[15] A. Borji, M. Cheng, H. Jiang and J. Li, Salient object detection: A survey, *arXiv Preprint*, arXiv: 1411.5878, 2014.

[16] A. Borji, M. Cheng, H. Jiang and J. Li, Salient object detection: A benchmark, *IEEE Transactions on Image Processing*, vol.24, no.12, pp.5706-5722, 2015.

[17] M. Cheng, G. Zhang, N. Mitra et al., Global contrast based salient region detection, *Proc. of IEEE Conference on Computer Vision and Pattern Recognition*, Colorado Springs, CO, USA, pp.409-416, 2011.

[18] Y. Wei, F. Wen, W. Zhu and J. Sun, Geodesic saliency using background priors, *Proc. of European Conference on Computer Vision*, Firenze, Italy, pp.29-42, 2012.

[19] C. Zhu, G. Li, W. Wang and R. Wang, An innovative salient object detection using center-dark channel prior, *Proc. of IEEE International Conference on Computer Vision Workshop*, Venice, Italy, pp.1509-1515, 2017.

[20] L. Itti, C. Koch and E. Niebur, A model of saliency-based visual attention for rapid scene analysis, *IEEE Transactions on Pattern Analysis and Machine Intelligence*, vol.20, no.11, pp.1254-1259, 1998.

[21] R. Achanta, S. Hemami, F. Estrada and S. Susstrunk, Frequency-tuned salient region detection, *Proc. of IEEE Conference on Computer Vision and Pattern Recognition*, Miami, FL, USA, pp.1597-1604, 2009.

[22] S. Goferman, L. Zelnik-Manor and A. Tal, Context-aware saliency detection, *IEEE Transactions on Pattern Analysis and Machine Intelligence*, vol.34, no.10, 2012.

[23] B. Jiang, L. Zhang, H. Lu et al., Saliency detection via absorbing Markov chain, *Proc. of IEEE International Conference on Computer Vision*, Sydney, NSW, Australia, pp.1665-1672, 2013.

[24] C. Yang, L. Zhang, H. Lu et al., Saliency detection via graph-based manifold ranking, *Proc. of IEEE Conference on Computer Vision and Pattern Recognition*, Portland, OR, USA, pp.3166-3173, 2013.

[25] Q. Wang, W. Zheng and R. Piramuthu, Grab: Visual saliency via novel graph model and background priors, *Proc. of IEEE Conference on Computer Vision and Pattern Recognition*, Las Vegas, NV, USA, pp.535-543, 2016.

[26] N. Tong, H. Lu, X. Ruan and M.-H. Yang, Salient object detection via bootstrap learning, *Proc. of IEEE Conference on Computer Vision and Pattern Recognition*, Boston, MA, USA, pp.1884-1892, 2015.

[27] X. Shen and Y. Wu, A unified approach to salient object detection via low rank matrix recovery, *Proc. of IEEE Conference on Computer Vision and Pattern Recognition*, Providence, RI, USA, pp.853-860, 2012.

[28] M. Yao, J. Li and X. Wang, Solar cells surface defects detection using RPCA method, *Chinese Journal of Computers*, vol.36, no.9, pp.1943-1952, 2013.

[29] Q. Huangpeng, H. Zhang, X. Zeng and W. Huang, Automatic visual defect detection using texture prior and low-rank representation, *IEEE Access*, vol.6, pp.37965-37976, 2018.

[30] J. Cao, N. Wang, J. Zhang et al., Detection of varied defects in diverse fabric images via modified RPCA with noise term and defect prior, *International Journal of Clothing Science and Technology*, vol.28, no.4, pp.516-529, 2016.

[31] S. Zhou, S. Wu, H. Liu et al., Double low-rank and sparse decomposition for surface defect segmentation of steel sheet, *Applied Sciences*, vol.8, no.9, pp.1-16, 2018.

[32] E. Candes, X. Li, Y. Ma and J. Wright, Robust principal component analysis?, *Journal of the ACM*, vol.58, no.3, pp.1-37, 2011.

[33] Z. Lin, M. Chen and Y. Ma, The augmented Lagrange multiplier method for exact recovery of corrupted low-rank matrices, *arXiv Preprint*, arXiv: 1009.5055v3, 2013.

[34] R. Achanta, A. Shaji, K. Smith et al., SLIC superpixels compared to state-of-the-art superpixel methods, *IEEE Transactions on Pattern Analysis and Machine Intelligence*, vol.34, no.11, pp.2274-2282, 2012.

[35] W. Zhu, S. Liang, Y. Wei and J. Sun, Saliency optimization from robust background detection, *Proc. of IEEE Conference on Computer Vision and Pattern Recognition*, Columbus, OH, USA, pp.2814-2821, 2014.

[36] N. Otsu, A threshold selection method from gray-level histograms, *IEEE Transactions on Systems, Man, and Cybernetics*, vol.9, no.1, pp.62-66, 1979.

[37] C. Tang, P. Wang, C. Zhang and W. Li, Salient object detection via weighted low rank matrix recovery, *IEEE Signal Processing Letters*, vol.24, no.4, pp.490-494, 2017.

[38] N. Imamoglu, W. Lin and Y. Fang, A saliency detection model using low-level features based on wavelet transform, *IEEE Transactions on Multimedia*, vol.15, no.1, pp.96-105, 2013.

[39] X. Hou and L. Zhang, Saliency detection: A spectral residual approach, *Proc. of IEEE Conference on Computer Vision and Pattern Recognition*, Minneapolis, MN, USA, pp.1-8, 2007.

[40] H. Tian, Y. Fang, Y. Zhao et al., Salient region detection by fusing bottom-up and top-down features extracted from a single image, *IEEE Transactions on Image Processing*, vol.23, no.10, pp.4389-4398, 2014.

[41] H. Tang, C. Chen and X. Pei, Visual saliency detection via sparse residual and outlier detection, *IEEE Signal Processing Letters*, vol.23, no.12, pp.1736-1740, 2016.

[42] R. Margolin, L. Zelnik-Manor and A. Tal, How to evaluate foreground maps, *Proc. of IEEE Conference on Computer Vision and Pattern Recognition*, Columbus, OH, USA, pp.248-255, 2014.